

1      **Estimating the impact of a major hurricane on**  
2      **transport processes**

3      Thomas Dobbelaere, Emmanuel Hanert

4      February 23, 2021

5      **Abstract**

6      In most hydrodynamic model studies, currents and waves are simu-  
7      lated separately. This is especially true for the simulation of passive  
8      drifters, whose trajectories are often computed based solely on cur-  
9      rents. Although this simplification holds for most situations, as the force  
10     exerted by waves on currents can be neglected in fair weather condi-  
11     tions, it may lead to significant errors during storm conditions, when  
12     currents are strongly influenced by wind-generated waves. In this study,  
13     we investigate current-wave interactions in heavy-wind conditions by  
14     coupling the unstructured-mesh hydrodynamic model SLIM with the  
15     wave model SWAN. We apply the coupled model in the Florida Reef  
16     Tract during Hurricane Irma (Sep. 2017) and show that it successfully  
17     reproduces both the observed wave behavior and storm surge during  
18     the hurricane. The modeled currents were then used to simulate the  
19     trajectories of passive drifters during the passage of the hurricane. Our  
20     results show that taking wave force into account induces variations of  
21     up 1 m/s in modelled currents on the continental shelf break as well  
22     as in the vicinity of reefs and islands. Wave-current interactions can  
23     therefore deflect the trajectories of drifting material by up to 10 km on  
24     the passage of the storm **Add something?**. These results strongly advo-  
25     cate for the inclusion of wave forces while studying transport processes  
26     (sediments, pollutants, larvae, etc.) in heavy-wind conditions.

<sup>27</sup> **1 Introduction**

<sup>28</sup> Wave-current interactions in coastal areas are of great importance for coastal  
<sup>29</sup> engineering as they play a key role in sediment transport, morphological  
<sup>30</sup> evolution and pollutant mixing (Bever and MacWilliams, 2013; Li and Johns,  
<sup>31</sup> 1998). However, these interactions are highly nonlinear and can vary sig-  
<sup>32</sup> nificantly in space and time (Wu et al., 2011). Wave-induced currents are  
<sup>33</sup> generated by wave radiation gradients (Longuet-Higgins, 1970), affecting  
<sup>34</sup> water levels near shorelines and wave breaking points (Longuet-Higgins  
<sup>35</sup> and Stewart, 1964), while changes in water levels and currents, in turn,  
<sup>36</sup> affect the motion and evolution of the waves (Sikirić et al., 2013). Cou-  
<sup>37</sup> pled wave-current models are therefore required to capture these complex  
<sup>38</sup> interactions.

<sup>39</sup> As coastal oceans are characterized by complex topology with islands,  
<sup>40</sup> inlets and estuaries, unstructured (usually two-dimensional) models are pre-  
<sup>41</sup> ferred as structured grid models show limitations in resolving topologically-  
<sup>42</sup> controlled nearshore processes (Wu et al., 2011; Chen et al., 2007). The  
<sup>43</sup> effect of wave-interactions becomes even more significant in the case of  
<sup>44</sup> hurricanes, that generate large wind-waves and disturb ocean conditions  
<sup>45</sup> (Liu et al., 2020) by causing coastal upwellings on continental shelves  
<sup>46</sup> (Smith, 1982) and inducing strong currents, waves and storm surges in  
<sup>47</sup> nearshore and coastal regions (Dietrich et al., 2010; Weisberg and Zheng,  
<sup>48</sup> 2006). South Florida and the Gulf of Mexico are particularly vulnerable to  
<sup>49</sup> hurricanes (Malmstadt et al., 2009) and modelling studies predict tropical  
<sup>50</sup> cyclones to increase both in frequency and intensity in this region (Mar-  
<sup>51</sup> sooli et al., 2019; Knutson et al., 2010). Being able to accurately model  
<sup>52</sup> wave-current interactions in this area becomes thus critical.

<sup>53</sup> Individual-based modelling of particulates has been extensively used to  
<sup>54</sup> study the transport of drifting materials such as pollutants, sediments or  
<sup>55</sup> larvae (Garcia-Pineda et al., 2020; Liubartseva et al., 2018; Figueiredo et al.,  
<sup>56</sup> 2013; Frys et al., 2020). Although some of these studies take the impact  
<sup>57</sup> of waves into account by adding a Stokes drift velocity, *i.e.* the net drift of a  
<sup>58</sup> floating particle in the direction of the wave propagation (Van Den Bremer  
<sup>59</sup> and Breivik, 2018), to the Eulerian currents, they usually neglect the wave-  
<sup>60</sup> induced currents. Such practice is reasonable in the case of fair weather,

61 when wave-induced forces exerted on currents are relatively smaller, but  
62 might lead to significant inaccuracies during storm conditions. To assess  
63 the importance of wave-current interactions during a tropical cyclone, we  
64 investigated the transport of drifting particulates on the Florida shelf during  
65 Hurricane Irma, one of the strongest and costliest tropical cyclones on  
66 records in the Atlantic Basin (Chen et al., 2007), that made landfall in Florida  
67 in September 2017.

68 In this study, we developed an unstructured coupled wave-current model of  
69 South Florida to simulate the ocean circulation during hurricane Irma. Both  
70 modelled currents and waves were validated against field measurements  
71 and were then used to simulate the transport of drifting material in the  
72 Florida Keys and the Florida inner shelf during the storm. Model outputs  
73 were then compared with uncoupled simulation results in order to assess  
74 the impact of wave-induced forces and Stokes drift on the modelled currents  
75 and transports.

## 76 **2 Methods**

### 77 **2.1 Study area and observational data**

78 Large-scale ocean circulation around South Florida is dominated by the  
79 Florida Current (FC), which originates from the Loop Currents (LC) where it  
80 enters the Florida Straits from the Gulf of Mexico, and, downstream, forms  
81 the Gulf Stream. The FC is a major western boundary current character-  
82 ized by spatial variability and meandering, associated with the presence  
83 of cyclonic eddies between the core of the current and the complex reef  
84 topography of the Florida Reef Tract (FRT) (Lee et al., 1995; Kourafalou and  
85 Kang, 2012). The northern half of these reefs are made of early Holocene  
86 reef frameworks and indurated sand ridges while the southern part (the  
87 Florida Keys) is composed of a chain of limestone islands, fossilized rem-  
88 nants of ancient coral reefs and sand bars (Hoffmeister and Multer, 1968;  
89 Shinn, 1988; Lidz and Shinn, 1991). The variability of the FC extends over  
90 a large range of spatial and temporal scales, with periods of 30-70 days in  
91 the Lower Keys (Lee et al., 1995) and shorter periods of 2-21 days in the  
92 Upper Keys (Lee and Mayer, 1977), and exhibits significant seasonal and

93 interannual cycles (Johns and Schott, 1987; Lee and Williams, 1988; Schott  
94 et al., 1988). Circulation on the West Florida Shelf (WFS) on the other hand  
95 is forced by local winds and tidal fluctuations (Lee and Smith, 2002; Liu and  
96 Weisberg, 2012).

97 The state of the ocean around Florida is monitored by an extensive array  
98 of tide gauges, current meters and buoys. In this study, we used sea  
99 surface elevation measurements from the National Oceanic and Atmospheric  
100 Administrations (NOAA) Tides and Currents dataset. These measurements  
101 were taken at four locations: two in the Florida Keys (Key West and Vaca  
102 Key); one on the eastern coast of Florida (Key West); and one on the western  
103 coast (Naples). For the currents, we used ADCP measurements from  
104 the University of South Florida's College of Marine Science's (USF/CMS)  
105 Coastal Ocean Monitoring and Prediction System (COMPS) for the WFS  
106 (Weisberg et al., 2009). More specifically, we used measurements from  
107 moorings C10, C12 and C13, respectively located at the 25, 50, and 50  
108 m isobaths of the WFS (Liu et al., 2020). Finally, for the waves, we used  
109 measurements from four buoys of the NOAA's National Data Buoy Center  
110 (NDBC). Two on Florida's Eastern shelf and two on the WFS. The locations  
111 of all measurement stations are shown on Fig. 1

## 112 **2.2 Wind and atmospheric pressure during Hurricane Irma**

113 Irma made landfall in Florida on 10 September 2017 as a category 3 storm,  
114 first at Cudjoe Key (Florida Keys) and later on Marco Island, south to Naples  
115 (see hurricane track in Fig. 1). It then weakened to a category 2 storm as it  
116 moved further inland (Pinelli et al., 2018). The storm caused damages to  
117 up to 75% of the buildings at his landfall point in the Florida Keys, making it  
118 one of the strongest and costliest hurricanes on record in the Atlantic basin  
119 (Xian et al., 2018; Zhang et al., 2019). The strongest reported wind speed  
120 was 50 m/s on Marco Island while the highest recorded storm surge was  
121 2.3 m, although larger wind speed likely occurred in the Florida Keys (Pinelli  
122 et al., 2018) In order to reproduce the wind profile of Irma in our model,  
123 we used high-resolution H\*Wind wind fields (Powell et al., 1998). As these  
124 data represent 1-min averaged wind speeds, we multiplied them by a factor  
125 0.93 to obtain 10-min averaged wind speeds (Harper et al., 2010), which

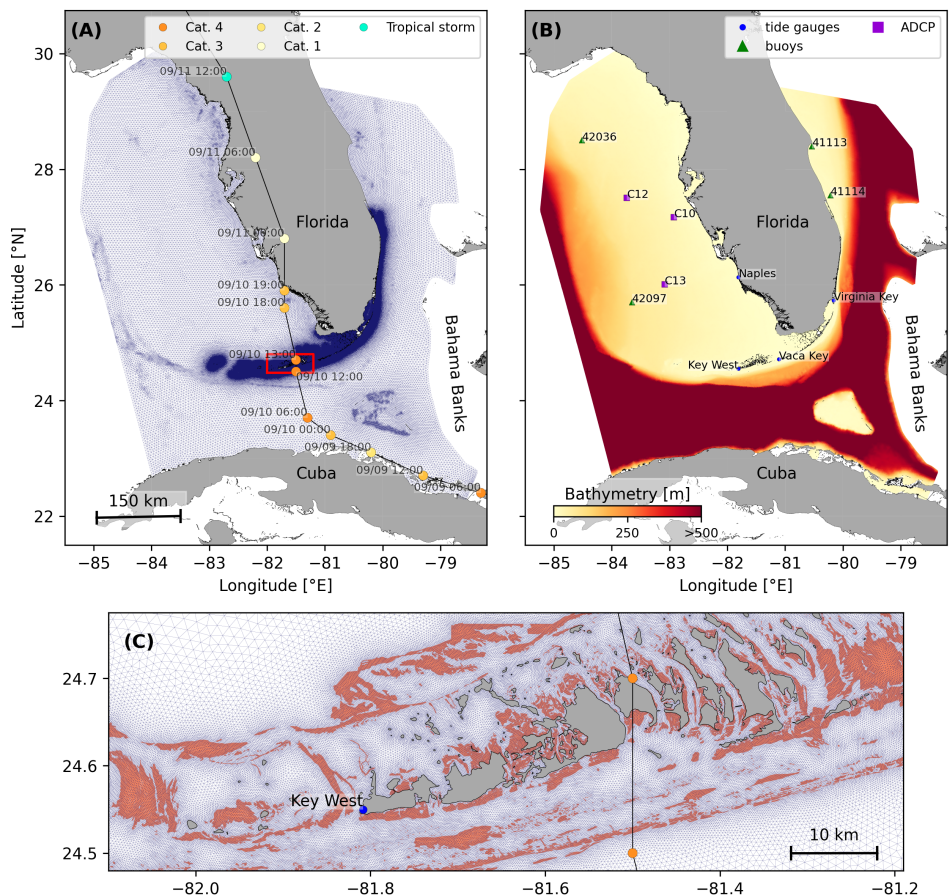


**Fig. 1:** **A:** Mesh of the computational domain with the trajectory of Irma, category of the hurricane is given by the Saffir-Simpson color scale. **B:** Bathymetry of the domain with the location of stations used for the validation of the model outputs. **C:** Close up view of the Lower Keys area, where the mesh resolution reaches 100m near reefs (shown in coral) and islands (highlighted in dark grey)

126 are more consistent with the time step of our model. Furthermore, H\*Wind  
 127 wind profiles did not cover the whole model extent during the hurricane and  
 128 were thus blended within coarser wind field extracted from ECMWF ERA-5  
 129 datasets. Pressure fields of Irma were also constructed using ERA-5 data.  
 130 However, the coarse resolution of the data set caused the depression at the  
 131 center of the hurricane to get smoothed out, leading to an underestimation of  
 132 the pressure gradient in our model. To better capture the central depression  
 133 of Irma, we built a hybrid pressure field using the position and the minimal  
 134 pressure of the core of the hurricane based on its track as recorded in  
 135 the HURDAT 2 database (Landsea and Franklin, 2013). Based on this  
 136 information, the hybrid pressure field was constructed by combining an  
 137 idealized Holland pressure profile (Lin and Chavas, 2012) within the radius  
 138 of maximum wind speed of Irma (Knaff et al., 2018) with ERA-5 pressure  
 139 field. The transition between from the Holland profile to ERA-5 data outside  
 140 the radius of maximum wind speed data was performed using a smooth step  
 141 function.

## 142 **2.3 Hydrodynamic model**

143 Ocean currents generated during hurricane Irma around South Florida were  
 144 modelled using the 2D barotropic version of the unstructured-mesh coastal  
 145 ocean model SLIM<sup>1</sup>. The model mesh covers an area similar to the model  
 146 extent of Dobbelaere et al. (2020b), that includes the FRT but also the Florida  
 147 Strait and part of the Gulf of Mexico (Figure 1). However, this area has  
 148 been slightly extended northeastward and westward in order to include the  
 149 NOAA-NDBC buoys. Furthermore, in order to withstand potential cell drying  
 150 during the hurricane, we solved the conservative shallow water equations  
 151 with wetting-drying:

$$\begin{aligned}
 \frac{\partial H}{\partial t} + \nabla \cdot (\mathbf{U}) &= 0, \\
 \frac{\partial \mathbf{U}}{\partial t} + \nabla \cdot \left( \frac{\mathbf{U}\mathbf{U}}{H} \right) &= -f \mathbf{e}_z \times \mathbf{U} + \alpha g H \nabla(H - h) - \frac{1}{\rho} \nabla p_{\text{atm}} + \frac{1}{\rho} \boldsymbol{\tau}_s \quad (1) \\
 &\quad + \nabla \cdot (\nu \nabla \mathbf{U}) - \frac{C_b}{H^2} |\mathbf{U}| \mathbf{U} + \gamma (\mathbf{U}_* - \mathbf{U}),
 \end{aligned}$$

---

<sup>1</sup><https://www.slim-ocean.be>

152 where  $H$  is the water column height and  $\mathbf{U}$  is the depth-averaged transport;  
 153  $f$  is the Coriolis coefficient;  $g$  is the gravitational acceleration;  $h$  is the  
 154 bathymetry;  $\alpha$  is a coefficient stating whether the mesh element is wet  
 155 ( $\alpha = 1$ ) or dry ( $\alpha = 0$ );  $\nu$  is the viscosity;  $C_b$  is the bulk bottom drag  
 156 coefficient;  $\nabla p_{\text{atm}}$  is the atmospheric pressure gradient;  $\tau_s$  is the surface  
 157 stress due to wind; and  $\gamma$  is a relaxation coefficient towards a reference  
 158 transport  $\mathbf{U}_*$ . As in Frys et al. (2020) and Dobbelaere et al. (2020b), SLIM  
 159 currents were gradually relaxed towards HYCOM (Chassignet et al., 2007) in  
 160 regions where the water depth exceeds 50m.

161 At very high wind speeds, the white cap is blown off the crest of the waves,  
 162 which generates a layer of droplets that acts as a slip layer for the winds  
 163 at the ocean-atmosphere interface (Holthuijsen et al., 2012). This causes  
 164 a saturation of the wind drag coefficient for strong winds (Donelan et al.,  
 165 2004; Powell et al., 2003). To account for the impact of this saturation  
 166 on the surface wind stress in our model, we implemented the wind drag  
 167 parameterization of Moon et al. (2007). In this parameterization, the drag  
 168 coefficient  $C_d$  depends on the wind speed at 10-m height  $U_{10}$  according to:

$$C_d = \kappa^2 \log \left( \frac{10}{z_0} \right)^{-2} \quad (2)$$

169 where  $\kappa$  is the von Karman constant. The roughness length  $z_0$  in Eq. (2) is  
 170 expressed as:

$$z_0 = \begin{cases} \frac{0.0185}{g} U_*^2 & \text{if } U_{10} \leq 12.5 \text{ m/s ,} \\ [0.085(-0.56U_*^2 + 20.255U_* + 2.458) - 0.58] \times 10^{-3} & \text{if } U_{10} > 12.5 \text{ m/s ,} \end{cases} \quad (3)$$

171 with  $U_*$  the friction velocity. The relation between  $U_{10}$  and  $U_*$  is given by:

$$U_{10} = -0.56U_*^2 + 20.255U_* + 2.458 . \quad (4)$$

172 The mesh resolution depends on the distance to coastlines and reefs follow-  
 173 ing the approach of (Dobbelaere et al., 2020b). The mesh was then further  
 174 refined as a function of bathymetry and bathymetry gradient, as suggested

175 by SWAN documentation<sup>2</sup>. Such approach improves the efficiency of the  
 176 computational grid by locally increasing the mesh resolution in areas where  
 177 the bathymetry or evolution of the waves change rapidly while avoiding to  
 178 invest too many computational resources where the physics or depth change  
 179 less. The mesh was generated using the Python library seamsh<sup>3</sup>, based  
 180 on the open-source mesh generator GMSH (Geuzaine and Remacle,  
 181 2009). It is composed of approximately  $7.7 \times 10^5$  elements. The coarsest  
 182 elements, far away from the FRT, had a characteristic length size of about 5  
 183 km whereas the finest elements had a characteristic length of 100 m near  
 184 coastlines and reefs (Fig 1).

## 185 **2.4 Wave model**

186 Waves were modelled using the parallel unstructured-mesh version of the  
 187 Simulating WAves Nearshore (SWAN) model (Booij et al., 1999), one of the  
 188 most commonly used wave models in coastal areas and inland waters. This  
 189 model solves the action balance equation, which reads (Mei, 1989):

$$\frac{\partial N}{\partial t} + \nabla_x \cdot [(c_g + \mathbf{u})N] + \frac{\partial}{\partial \theta}[c_\theta N] + \frac{\partial}{\partial \sigma}[c_\sigma N] = \frac{S_{in} + S_{ds} + S_{nl}}{\sigma}, \quad (5)$$

190 where  $N = E/\sigma$  is the wave action density;  $\theta$  is the wave propagation  
 191 direction;  $\sigma$  is the wave relative frequency;  $c_g$  is the wave group velocity,  
 192  $\mathbf{u} = \mathbf{U}/H$  is SLIM depth-averaged current velocity;  $c_\theta$  and  $c_\sigma$  are the propa-  
 193 gation velocities in spectral space due to refraction and shifting in frequency  
 194 due to variations in depth and currents; and  $S_{in}$ ,  $S_{ds}$ , and  $S_{nl}$  respectively  
 195 represent wave growth by wind, wave decay and nonlinear transfers of  
 196 wave energy through interactions between triplets and quadruplets. Spectra  
 197 were discretized with 48 direction bins and 50 frequency bins logarithmically  
 198 distributed from 0.3 to 2 Hz. Exponential wind growth was parameterized  
 199 using the formulation of Janssen (1991), while dissipations by whitecapping  
 200 and bottom dissipations followed the formulations of Komen et al. (1984)  
 201 and Madsen et al. (1989) respectively. Coefficients for exponential wind  
 202 growth and whitecapping parameterizations were based on the results of  
 203 Siadatmousavi et al. (2011), and significantly differ from SWAN's default

---

<sup>2</sup><http://swanmodel.sourceforge.net/unswan/unswan.htm>

<sup>3</sup><https://pypi.org/project/seamsh/>

204 settings. By default, SWAN implements the wind input formulation of Komen  
 205 et al. (1984) and the steepness-dependent coefficient governing dissipation  
 206 by whitecapping is a linear function of the wave number. In this study, this  
 207 steepness-dependent coefficient is a quadratic function of the wave number,  
 208 as it showed better predictions of the significant wave height in the study of  
 209 Siadatmousavi et al. (2011). The choice of these formulations was motivated  
 210 by the appearance of numerical instabilities in the region of the Gulf Stream  
 211 using SWAN's default parameter values. Finally, wave boundary conditions  
 212 were derived from WAVEWATCH III (Tolman et al., 2009) spectral outputs at  
 213 buoy locations. Surface wave induce a net drift in te direction of the wave  
 214 propagation, known as Stokes drift (Van Den Bremer and Breivik, 2018;  
 215 Stokes, 1880). This net drift has significant impacts on sediment motion  
 216 in near shore regions (Hoefel and Elgar, 2003), the formation of Langmuir  
 217 cells (Langmuir, 1938; Craik and Leibovich, 1976) as well as the transport of  
 218 heat, salt or pollutants such as oil or micro-plastic in the upper ocean layer  
 219 (McWilliams and Sullivan, 2000; Röhrs et al., 2012; Drivedal et al., 2014).  
 220 To model adequately the Stokes profile in mixed wind-driven sea and swell  
 221 conditions, the full two- dimensional wave spectrum must be represented  
 222 by a spectral wave model within a wave-current coupling (Van Den Bremer  
 223 and Breivik, 2018). In this study, depth-averaged Stokes drift was therefore  
 224 computed by SWAN using the following formula:

$$\mathbf{u}_s = \int_0^{2\pi} \int_0^{+\infty} \frac{\sigma^3}{h \tanh(2kh)} E(\sigma, \theta) (\cos \theta, \sin \theta) d\sigma d\theta , \quad (6)$$

225 where  $k$  is the norm of the wave vector;  $h$  is the water depth; and  $E(\sigma, \theta)$  is  
 226 the wave energy density.

## 227 2.5 Coupled model

228 SLIM and SWAN are coupled so that they run on the same computational  
 229 core and the same unstructured mesh. SLIM is run first and passes com-  
 230 puted wind velocities ( $\mathbf{U}_{10}$ ), water levels ( $\eta = H - h$ ) and depth-averaged  
 231 currents ( $\mathbf{u} = \mathbf{U}/H$ ) to SWAN, as well as a roughness length ( $z_0$ ) for the bot-  
 232 tom dissipation formulation of Madsen et al. (1989). This roughness length  
 233 is computed from SLIM's bulk drag coefficient  $C_b$  following the approach of  
 234 Dietrich et al. (2011) so that both models have consistent bottom dissipation

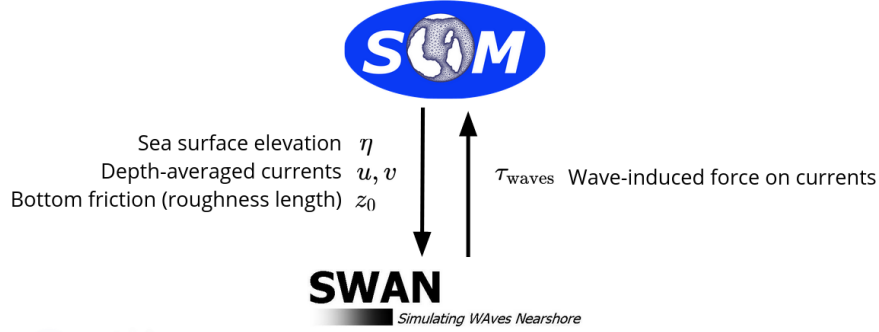


**Fig. 2:** Schematic illustration of the coupled SLIM+SWAN model.

parameterizations. SWAN then utilizes these quantities to compute the wave radiation stress gradient, that is then passed to SLIM as the wave-induced stress on currents  $\tau_{\text{wave}}$ . SLIM then uses this quantity to update the value of the surface stress  $\tau_s$  in Eq. (1), that now becomes the sum of wind and wave-induced stresses  $\tau_s = \tau_{\text{wind}} + \tau_{\text{wave}}$ .

SLIM equations are integrated using an implicit scheme while SWAN is unconditionally stable (Dietrich et al., 2010), allowing both models to be run with relatively large time steps. In this study, both models were therefore run sequentially using a time step of 600s, so that each computational core was alternating running either SLIM or SWAN. As in the coupling between SWAN and ADCIRC (Dietrich et al., 2010), both models utilize the same local sub-mesh, allowing for a one-to-one correspondence between the geographic locations of the mesh vertices. No interpolation is therefore needed when passing computed quantities from a model to another, which allows for efficient inter-model communication. However, as SLIM applies discontinuous Galerkin finite element methods, an additional conversion step to a continuous framework was required to transmit SLIM nodal quantities to SWAN.

### 3 Results

We first validated the reconstructed atmospheric fields of hurricane Irma as well the modelled currents and waves of our coupled model against fields measurements. Once we had built some confidence in our model accuracy

257 we used these, we used these modelled quantities to represent the transport  
258 of passive particles in the Lower Florida Keys during the passage of the  
259 hurricane. These transports were obtained using three data sets: (i) currents  
260 from an uncoupled SLIM simulation of Irma (SLIM); (ii) currents modelled  
261 by the coupled SLIM+SWAN model (SLIM+SWAN); (iii) currents modelled  
262 by the coupled SLIM+SWAN model to which the modelled depth-averaged  
263 Stokes drift was added (Eq. 6) (SLIM+SWAN+Stokes). We then compared  
264 the particle trajectories obtained with these three sets of currents to assess  
265 the impact of wave-current coupling on drifter transport during the passage  
266 of a major hurricane.

### 267 **3.1 Model validation**

268 H\*Wind winds and hybrid pressure field agree well with station measure-  
269 ments at Vaca Key station (Fig. 3). The hybrid pressure field shows better  
270 agreement with observations than ERA-5 pressure as it successfully re-  
271 produces the storm depression. ERA-5 fields, on the other hand, fail to  
272 resolve the low pressure at the core of the hurricane due to their coarser  
273 grid, leading to an overestimation of 8 mbar of the storm depression. Both  
274 H\*Wind and ERA-5 agree well with observed wind speeds although both  
275 data sets tend to slightly overestimate the width and intensity of the wind  
276 peak. However, H\*wind profiles show a better match with the timing of the  
277 observed peak, as ERA-5 winds tend to anticipate it. H\*wind also exhibits a  
278 slightly narrower peak in wind speed, which better agrees with observations.  
279 Hydrodynamic outputs of the coupled wave-current agree well with tide  
280 gauge (Fig. 4) and ADCP measurements (Fig. 5). The timing and amplitude  
281 of the storm surges are well reproduced by the coupled model, the largest  
282 model error being an overestimation of 18 cm of the elevation peak at  
283 Virginia Key. The fit is especially good at Naples, where both the positive  
284 and negative surges are captured by the coupled model with an error of less  
285 than 5 cm. This result is of interest as negative surges, although less studied,  
286 affect water exchanges between the estuaries and the coastal ocean and  
287 disturb the benthic ecosystems (Liu et al., 2020). Modelled 2D currents were  
288 validated against depth-averaged ADCP measurements at mooring station  
289 C10, C12 and C13 (Fig. 5). As in Liu et al. (2020), the vector correlation

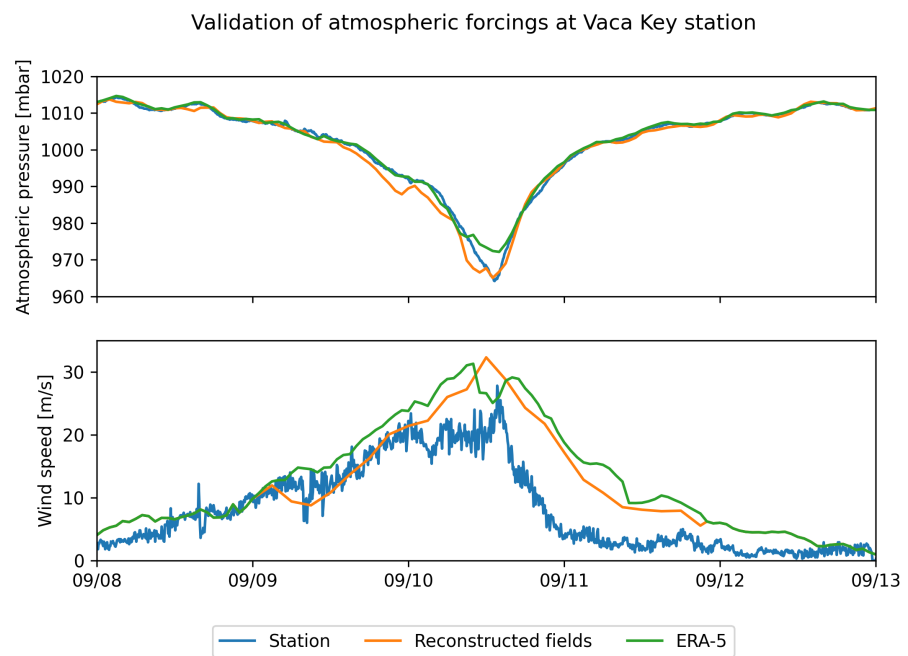


**Fig. 3:** Comparison of reconstructed wind atmospheric pressure with field measurements and coarser ECMWF ERA-5 profiles at Vaca Key station. The generated hybrid atmospheric forcings better capture the observed storm depression while H\*wind winds better match the measured peak in wind speed.

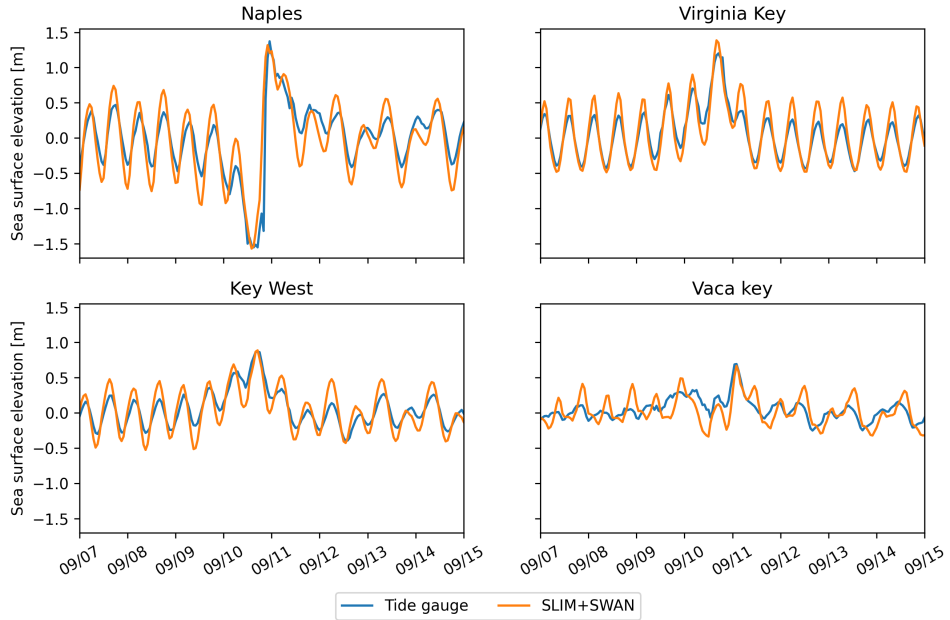


**Fig. 4:** Comparison of modelled sea surface elevation with all 4 tide gauge measurements (see Fig. 1B for their location). Timing and amplitudes of the storm surges are well reproduced by the model

analysis of Kundu (1976) is performed to compare modelled and observed current velocity vectors. Correlation coefficients ( $\rho$ ) between simulated and observed depth-averaged currents were 0.84, 0.74 and 0.73 at the C10, C12 and C13 locations, respectively. Average veering angles were computed as well and were below  $12^\circ$ , as in (Liu et al., 2020). However, in our case, no clear tendency regarding modelled current behavior compared to observations was observed. As expected from a depth-averaged model, the best fit with observations is obtained at the shallowest mooring C10, located on the 25m isobath, with an average veering angle of  $6^\circ$ .

The simulated significant wave height agrees well with observations on the WFS, where errors on the peak value do not exceed 5%. On the East Florida Shelf, errors are slightly larger reaching 20%. Although the model outputs agree well with observations, a lag in significant wave height is observed for all 4 buoys. Moreover, the peak in significant wave height tends to be underestimated at buoys 41113 and 41114, located on the East Florida Shelf. Other wave parameters were better reproduced by the model on the WFS as well, as illustrated for buoy 42036 in Fig. 6. This good fit on the WFS is not

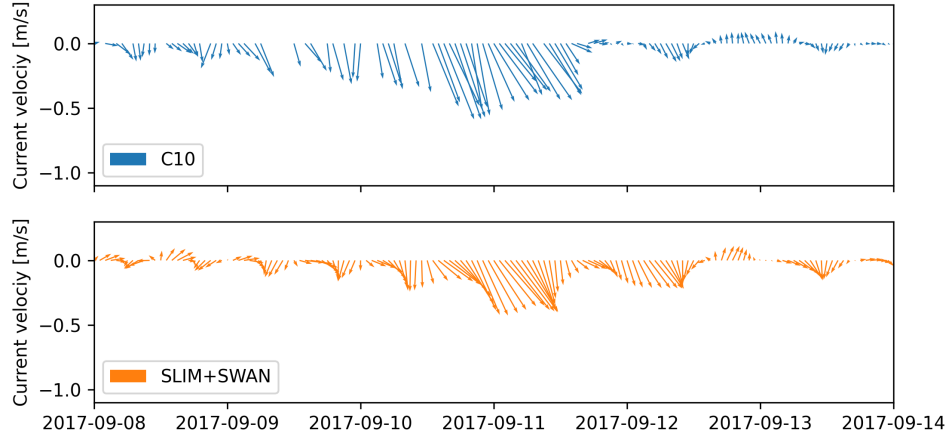


**Fig. 5:** Comparison of modelled current velocity with observed velocity at mooring C10 (see Fig. 1B for its location). Modelled current velocities agree well with observations, with a correlation coefficient of 0.83 and an average veering angle of  $6^\circ$ .

surprising as the parameters used for wind energy input and whitecapping dissipation were based on the calibration performed by (Siadatmousavi et al., 2011) on the Northern Gulf of Mexico. Wind-induced wave growth might therefore be underestimated on the eastern shelf. Consequently, incident wave do not receive enough energy to grow after breaking on the bank boundary, leading to an underestimation of the significant wave height at the location of the buoys. Nonetheless, as this study focused on the wave produced by Irma, that made landfall on the western coasts of Florida, the use of parameterizations calibrated for the Gulf of Mexico seems reasonable.

### 3.2 Impact of waves on currents and transport

We evaluated the impact of wave-current interactions on modelled currents during the passage of Irma in the Lower Keys, between the 7 September and the 13 September 2017. First, we computed the maximum difference between currents modelled by SLIM and SLIM+SWAN during this period (Fig. 7A). The largest differences in currents were observed over reefs, on the shelf break and around islands and can reach 1 m/s, with SLIM+SWAN currents having the largest amplitude. These areas of strong current differences correspond to the regions where the largest wave-induced stress

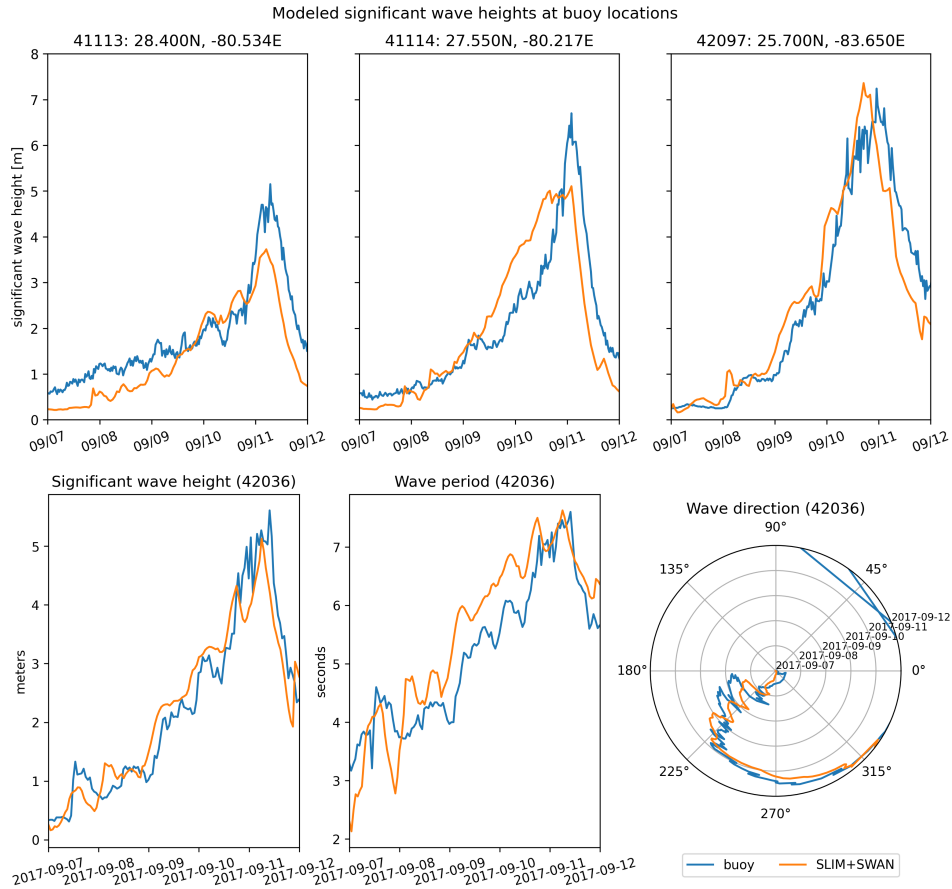


**Fig. 6:** Comparison of modelled wave parameters with observation at the 4 buoys location (locations shown in Fig. 1B). Modelled significant wave height agrees well with field measurement. As model parameters were calibrated for the Northern Gulf of Mexico, observations are better reproduced at buoys located on the WFS, as illustrated for buoy 42036

325  $\tau_{\text{wave}}$  occurred (7B), as wave breaking and wave slowing down over rough  
326 seabed induce variations of the wave radiation stress (Longuet-Higgins and  
327 Stewart, 1964). Wave-induced differences in current velocity were amplified  
328 by the action of the wind stress  $\tau_{\text{wind}}$  (Fig. 7C). Wind speeds were larger in  
329 the front right quadrant of the hurricane (Zedler et al., 2009), causing the  
330 difference in current velocities to be larger on the right side of the storm  
331 trajectory. This is especially clear in the area between the Florida Keys  
332 and the Everglades, where relatively small values of the radiation stress  
333 gradient produced strong differences in current velocity of up to 0.5 m/s in  
334 combination with the action of the winds.

335 To quantify the impact of these differences in velocity fields, we compared  
336 the trajectories of virtual particles driven by currents produced by SLIM  
337 alone and SLIM+SWAN simulations in the Florida Keys. First, we identified  
338 the areas where the differences between the modelled currents were the  
339 largest. Then, we determined the potential origination regions of particles  
340 reaching these areas on the passage of the hurricane through the Florida  
341 Keys using backtracking methods (Dobbelaere et al., 2020a). These regions  
342 are highlighted by the 4 release regions of Fig. 8. Finally, particles were  
343 released from these four regions and advected by currents produced by the  
344 coupled and uncoupled models. At each time step, the center of mass of  
345 the modelled particle clouds were computed. The distance between these  
346 centers of mass was used as a measure of the impact of the wind-generated  
347 wave coupling on the modelled current in the Florida Keys during hurricane  
348 Irma. This comparison was performed with 3 sets of currents: the currents  
349 modelled by uncoupled SLIM (SLIM); the currents modelled by coupled  
350 SLIM+SWAN (SLIM+SWAN); and the SLIM+SWAN currents with depth-  
351 averaged Stokes drift (SLIM+SWAN+Stokes) [sentence is too condensed].  
352 The results of these comparisons are shown in Fig. 8 [reformulate as active  
353 sentence]. Differences between the modelled trajectories are negligible  
354 before the passage of the hurricanes in the Florida Keys. Then, distance  
355 between the centers of mass of the particles abruptly increase to up to  
356 tens of kilometers as Irma gets through the Keys to finally stabilize after  
357 the passage of the hurricane. These results support the assumption that  
358 wave-induced transport is negligible compared to advection by Eulerian  
359 currents in fair weather conditions. Particles advected by the currents of  
360 the coupled model tend to remain on the shelf while particles advected by

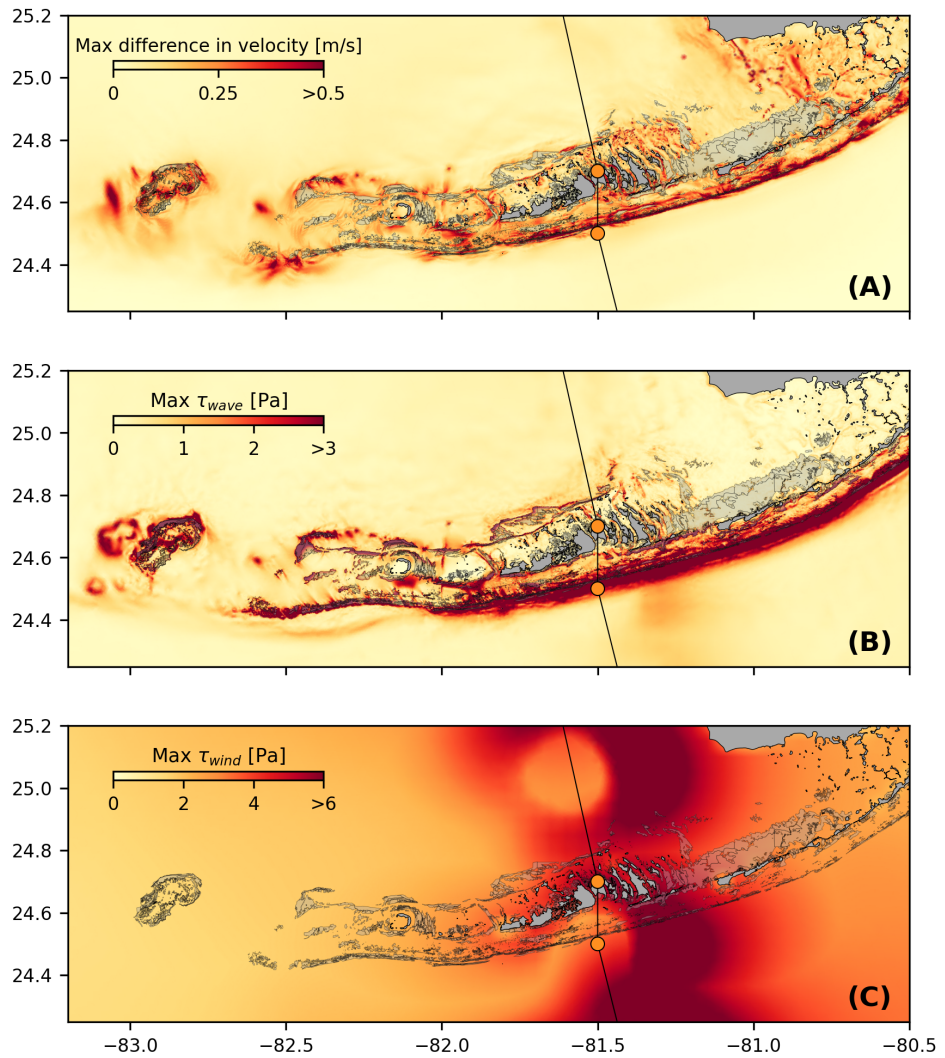


**Fig. 7:** Maximum difference between SLIM and SLIM+SWAN currents (A) during the passage of Irma in the Lower Florida Keys, along with the maximum wave radiation stress gradient  $\tau_{wave}$  (B) and wind stress  $\tau_{wind}$  (C) generated by the hurricane. Wave-induced stress yields difference larger than 0.5 m/s in current velocities. These wave-induced differences in currents were amplified by the action of the asymmetric wind profile of Irma, with larger differences occurring on the right of the storm trajectory

361 SLIM alone are mostly transported along the shelf break. Although not  
362 shown in this paper, comparison of SLIM and SLIM+SWAN trajectories were  
363 conducted as well. The evolution of the distance between centers of mass  
364 of the particle clouds showed similar trends while yielding smaller values.  
365 Modelled maximal depth-averaged Stokes drift reached up to 0.2 m/s during  
366 the passage of Irma through the Florida Keys. This suggests that both the  
367 impact of wave-induced force on Eulerian currents and Stokes drift should be  
368 taken into account while modelling particle transport under storm conditions.

## 369 **4 Discussion and conclusions**

370 Impact of waves on coral connectivity  
371 Ability of wave model to correctly capture gradient in significant wave height  
372 due to current-waves interactions under tropical cyclones depends on:

- 373     • Broad perspective  $\Rightarrow$  not limited to FL
- 374     • Mention search and rescue
- 375     • However, ignoring waves in storm conditions could result in significant  
376       inaccuracies in modelled trajectories, as illustrated in the case of  
377       release region 2 in Fig. 8
- 378     • Spatial (10km  $\rightarrow$  5km) and spectral (36 dir.  $\rightarrow$  48 dir.) resolution  
379       (Hegermiller et al., 2019)
- 380     • Directional spreading of incident waves (Villas Bôas et al., 2020)

## 381 **Conflict of Interest Statement**

382 The authors declare that the research was conducted in the absence of any  
383 commercial or financial relationships that could be construed as a potential  
384 conflict of interest.

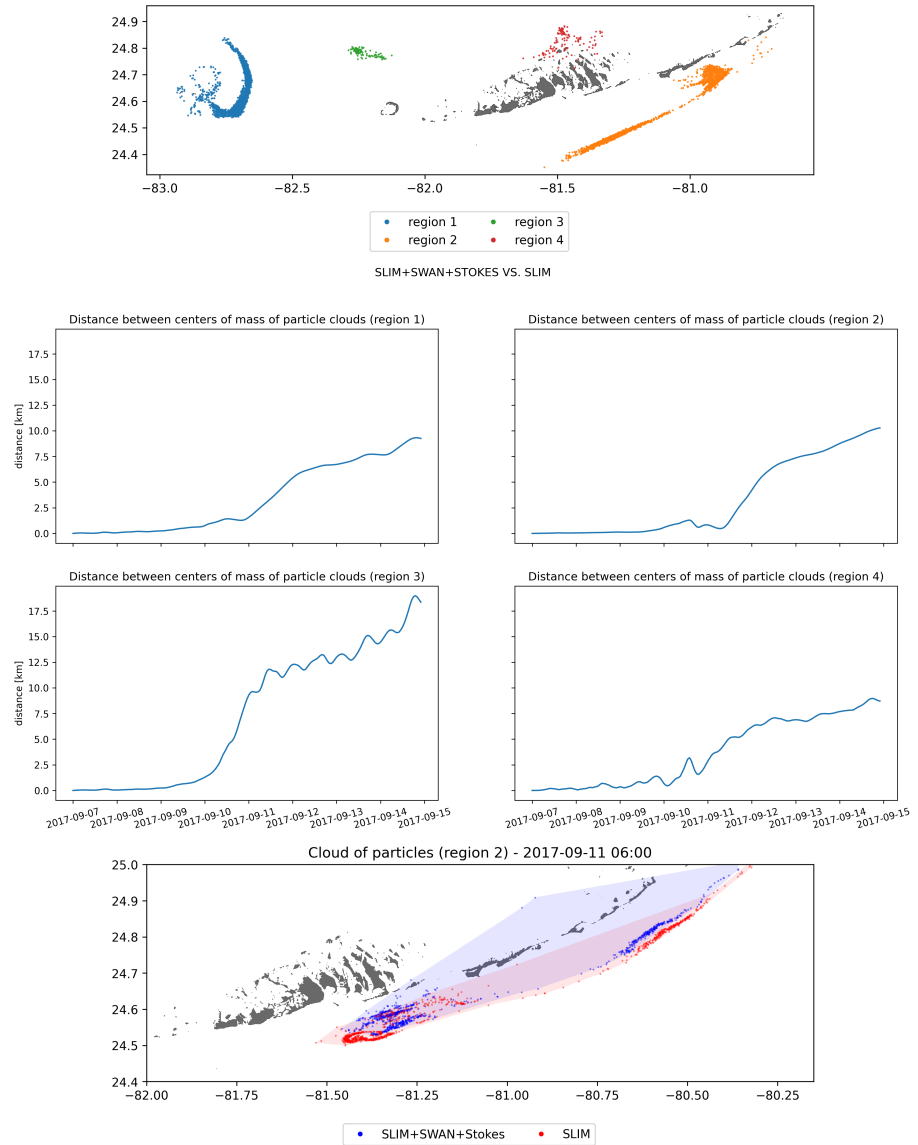


**Fig. 8:** Comparison of passive drifters trajectories with SLIM+SWAN+Stokes drift vs. SLIM alone. A snapshot of the positions of the particles released from region 2 is shown after the passage of Irma in the Florida Keys. Particles advected by the currents of the coupled model tend to remain on the shelf while particles advected by SLIM alone are mostly transported along the shelf break

<sup>385</sup> **Author Contributions**

<sup>386</sup> **Funding**

<sup>387</sup> **Acknowledgments**

<sup>388</sup> Computational resources were provided by the Consortium des Équipements  
<sup>389</sup> de Calcul Intensif (CÉCI), funded by the F.R.S.-FNRS under Grant No. 2.5020.11.  
<sup>390</sup> Thomas Dobbelaere is a PhD student supported by the Fund for Research  
<sup>391</sup> training in Industry and Agriculture (FRIA/FNRS).

<sup>392</sup> **Supplementary Material**

<sup>393</sup> The Supplementary Material for this article is attached to the submitted  
<sup>394</sup> document.

<sup>395</sup> **References**

- <sup>396</sup> Bever, A. J. and MacWilliams, M. L. (2013). Simulating sediment transport  
<sup>397</sup> processes in San Pablo Bay using coupled hydrodynamic, wave, and  
<sup>398</sup> sediment transport models. *Marine Geology*, 345:235–253.
- <sup>399</sup> Booij, N., Ris, R. C., and Holthuijsen, L. H. (1999). A third-generation wave  
400 model for coastal regions: 1. Model description and validation. *Journal  
401 of geophysical research: Oceans*, 104(C4):7649–7666.
- <sup>402</sup> Chassignet, E. P., Hurlbert, H. E., Smedstad, O. M., Halliwell, G. R., Hogan,  
403 P. J., Wallcraft, A. J., Baraille, R., and Bleck, R. (2007). The HYCOM  
404 (hybrid coordinate ocean model) data assimilative system. *Journal of  
405 Marine Systems*, 65(1-4):60–83.
- <sup>406</sup> Chen, C., Huang, H., Beardsley, R. C., Liu, H., Xu, Q., and Cowles, G. (2007).  
407 A finite volume numerical approach for coastal ocean circulation studies:  
408 Comparisons with finite difference models. *Journal of Geophysical  
409 Research: Oceans*, 112(C3).

- 410 Craik, A. D. and Leibovich, S. (1976). A rational model for Langmuir circula-  
411 tions. *Journal of Fluid Mechanics*, 73(3):401–426.
- 412 Dietrich, J., Bunya, S., Westerink, J., Ebersole, B., Smith, J., Atkinson,  
413 J., Jensen, R., Resio, D., Luettich, R., Dawson, C., et al. (2010). A  
414 high-resolution coupled riverine flow, tide, wind, wind wave, and storm  
415 surge model for southern Louisiana and Mississippi. part ii: Synoptic  
416 description and analysis of hurricanes Katrina and Rita. *Monthly Weather  
Review*, 138(2):378–404.
- 417
- 418 Dietrich, J., Westerink, J., Kennedy, A., Smith, J., Jensen, R., Zijlema, M.,  
419 Holthuijsen, L., Dawson, C., Luettich, R., Powell, M., et al. (2011).  
420 Hurricane Gustav (2008) waves and storm surge: Hindcast, synoptic  
421 analysis, and validation in southern Louisiana. *Monthly Weather Review*,  
422 139(8):2488–2522.
- 423
- 424 Dobbelaere, T., Muller, E., Gramer, L., Holstein, D., and Hanert, E. (2020a).  
425 Report on the potential origin of the SCTLD in the Florida Reef Tract.  
426 Available online at: [https://floridadep.gov/rcp/coral/documents/  
report-potential-origin-sctld-florida-reef-tract](https://floridadep.gov/rcp/coral/documents/report-potential-origin-sctld-florida-reef-tract).
- 427
- 428 Dobbelaere, T., Muller, E. M., Gramer, L. J., Holstein, D. M., and Hanert, E.  
429 (2020b). Coupled epidemic-hydrodynamic modeling to understand the  
430 spread of a deadly coral disease in Florida. *Frontiers in Marine Science*,  
7:1016.
- 431
- 432 Donelan, M., Haus, B., Reul, N., Plant, W., Stiassnie, M., Gruber, H., Brown,  
433 O., and Saltzman, E. (2004). On the limiting aerodynamic roughness of  
the ocean in very strong winds. *Geophysical Research Letters*, 31(18).
- 434
- 435 Drivdal, M., Broström, G., and Christensen, K. (2014). Wave-induced mixing  
436 and transport of buoyant particles: application to the Statfjord A oil spill.  
*Ocean Science*, 10(6):977–991.
- 437
- 438 Figueiredo, J., Baird, A. H., and Connolly, S. R. (2013). Synthesizing larval  
439 competence dynamics and reef-scale retention reveals a high potential  
for self-recruitment in corals. *Ecology*, 94(3):650–659.
- 440
- 441 Frys, C., Saint-Amand, A., Le Hénaff, M., Figueiredo, J., Kuba, A., Walker, B.,  
Lambrechts, J., Vallaeyns, V., Vincent, D., and Hanert, E. (2020). Fine-

- 442 scale coral connectivity pathways in the Florida Reef Tract: implications  
443 for conservation and restoration. *Frontiers in Marine Science*, 7:312.
- 444 Garcia-Pineda, O., Androulidakis, Y., Le Hénaff, M., Kourafalou, V., Hole,  
445 L. R., Kang, H., Staples, G., Ramirez, E., and DiPinto, L. (2020). Mea-  
446 suring oil residence time with GPS-drifters, satellites, and Unmanned  
447 Aerial Systems (UAS). *Marine pollution bulletin*, 150:110644.
- 448 Geuzaine, C. and Remacle, J.-F. (2009). Gmsh: A 3-d finite element mesh  
449 generator with built-in pre-and post-processing facilities. *International*  
450 *journal for numerical methods in engineering*, 79(11):1309–1331.
- 451 Harper, B., Kepert, J., and Ginger, J. (2010). *Guidelines for converting*  
452 *between various wind averaging periods in tropical cyclone conditions*.  
453 Citeseer.
- 454 Hegermiller, C. A., Warner, J. C., Olabarrieta, M., and Sherwood, C. R.  
455 (2019). Wave–current interaction between Hurricane Matthew wave  
456 fields and the Gulf Stream. *Journal of Physical Oceanography*,  
457 49(11):2883–2900.
- 458 Hoefel, F. and Elgar, S. (2003). Wave-induced sediment transport and  
459 sandbar migration. *Science*, 299(5614):1885–1887.
- 460 Hoffmeister, J. and Multer, H. (1968). Geology and origin of the Florida Keys.  
461 *Geological Society of America Bulletin*, 79(11):1487–1502.
- 462 Holthuijsen, L. H., Powell, M. D., and Pietrzak, J. D. (2012). Wind and waves  
463 in extreme hurricanes. *Journal of Geophysical Research: Oceans*,  
464 117(C9).
- 465 Janssen, P. A. (1991). Quasi-linear theory of wind-wave generation applied  
466 to wave forecasting. *Journal of physical oceanography*, 21(11):1631–  
467 1642.
- 468 Johns, W. E. and Schott, F. (1987). Meandering and transport variations  
469 of the Florida Current. *Journal of physical oceanography*, 17(8):1128–  
470 1147.
- 471 Knaff, J. A., Sampson, C. R., and Musgrave, K. D. (2018). Statistical tropi-  
472 cal cyclone wind radii prediction using climatology and persistence:

- 473      Updates for the western North Pacific. *Weather and Forecasting*,  
474      33(4):1093–1098.
- 475      Knutson, T. R., McBride, J. L., Chan, J., Emanuel, K., Holland, G., Landsea,  
476      C., Held, I., Kossin, J. P., Srivastava, A., and Sugi, M. (2010). Tropical  
477      cyclones and climate change. *Nature geoscience*, 3(3):157–163.
- 478      Komen, G., Hasselmann, S., and Hasselmann, K. (1984). On the exis-  
479      tence of a fully developed wind-sea spectrum. *Journal of physical*  
480      *oceanography*, 14(8):1271–1285.
- 481      Kourafalou, V. H. and Kang, H. (2012). Florida Current meandering and  
482      evolution of cyclonic eddies along the Florida Keys Reef Tract: Are they  
483      interconnected? *Journal of Geophysical Research: Oceans*, 117(C5).
- 484      Kundu, P. K. (1976). Ekman veering observed near the ocean bottom.  
485      *Journal of Physical Oceanography*, 6(2):238–242.
- 486      Landsea, C. W. and Franklin, J. L. (2013). Atlantic hurricane database un-  
487      certainty and presentation of a new database format. *Monthly Weather*  
488      *Review*, 141(10):3576–3592.
- 489      Langmuir, I. (1938). Surface motion of water induced by wind. *Science*,  
490      87(2250):119–123.
- 491      Lee, T. N., Leaman, K., Williams, E., Berger, T., and Atkinson, L. (1995).  
492      Florida Current meanders and gyre formation in the southern Straits  
493      of Florida. *Journal of Geophysical Research: Oceans*, 100(C5):8607–  
494      8620.
- 495      Lee, T. N. and Mayer, D. A. (1977). Low-frequency current variability and  
496      spin-off eddies along the shelf off southeast Florida. *Collected Reprints*,  
497      1(1):344.
- 498      Lee, T. N. and Smith, N. (2002). Volume transport variability through the  
499      Florida Keys tidal channels. *Continental Shelf Research*, 22(9):1361–  
500      1377.
- 501      Lee, T. N. and Williams, E. (1988). Wind-forced transport fluctuations of the  
502      Florida Current. *Journal of Physical Oceanography*, 18(7):937–946.

- 503 Li, Z. and Johns, B. (1998). A three-dimensional numerical model of surface  
504 waves in the surf zone and longshore current generation over a plane  
505 beach. *Estuarine, Coastal and Shelf Science*, 47(4):395–413.
- 506 Lidz, B. H. and Shinn, E. A. (1991). Paleoshorelines, reefs, and a rising sea:  
507 South florida, usa. *Journal of Coastal Research*, pages 203–229.
- 508 Lin, N. and Chavas, D. (2012). On hurricane parametric wind and appli-  
509 cations in storm surge modeling. *Journal of Geophysical Research: Atmospheres*, 117(D9).
- 511 Liu, Y. and Weisberg, R. H. (2012). Seasonal variability on the West Florida  
512 shelf. *Progress in Oceanography*, 104:80–98.
- 513 Liu, Y., Weisberg, R. H., and Zheng, L. (2020). Impacts of hurricane Irma  
514 on the circulation and transport in Florida Bay and the Charlotte Harbor  
515 estuary. *Estuaries and Coasts*, 43(5):1194–1216.
- 516 Liubartseva, S., Coppini, G., Lecci, R., and Clementi, E. (2018). Tracking  
517 plastics in the Mediterranean: 2D Lagrangian model. *Marine pollution  
518 bulletin*, 129(1):151–162.
- 519 Longuet-Higgins, M. S. (1970). Longshore currents generated by obliquely  
520 incident sea waves. *Journal of geophysical research*, 75(33):6778–  
521 6789.
- 522 Longuet-Higgins, M. S. and Stewart, R. (1964). Radiation stresses in water  
523 waves; a physical discussion, with applications. In *Deep sea research  
524 and oceanographic abstracts*, volume 11, pages 529–562. Elsevier.
- 525 Madsen, O. S., Poon, Y.-K., and Gruber, H. C. (1989). Spectral wave  
526 attenuation by bottom friction: Theory. In *Coastal Engineering 1988*,  
527 pages 492–504.
- 528 Malmstadt, J., Scheitlin, K., and Elsner, J. (2009). Florida hurricanes and  
529 damage costs. *southeastern geographer*, 49(2):108–131.
- 530 Marsooli, R., Lin, N., Emanuel, K., and Feng, K. (2019). Climate change  
531 exacerbates hurricane flood hazards along US Atlantic and Gulf Coasts  
532 in spatially varying patterns. *Nature communications*, 10(1):1–9.

- 533 McWilliams, J. C. and Sullivan, P. P. (2000). Vertical mixing by Langmuir  
534 circulations. *Spill Science & Technology Bulletin*, 6(3-4):225–237.
- 535 Mei, C. C. (1989). *The applied dynamics of ocean surface waves*, volume 1.  
536 World scientific.
- 537 Moon, I.-J., Ginis, I., Hara, T., and Thomas, B. (2007). A physics-based  
538 parameterization of air–sea momentum flux at high wind speeds and  
539 its impact on hurricane intensity predictions. *Monthly weather review*,  
540 135(8):2869–2878.
- 541 Pinelli, J.-P., Roueche, D., Kijewski-Correa, T., Plaz, F., Prevatt, D., Zisis,  
542 I., Elawady, A., Haan, F., Pei, S., Gurley, K., et al. (2018). Overview  
543 of damage observed in regional construction during the passage of  
544 Hurricane Irma over the State of Florida. In *Forensic Engineering 2018:*  
545 *Forging Forensic Frontiers*, pages 1028–1038. American Society of  
546 Civil Engineers Reston, VA.
- 547 Powell, M. D., Houston, S. H., Amat, L. R., and Morisseau-Leroy, N. (1998).  
548 The HRD real-time hurricane wind analysis system. *Journal of Wind  
549 Engineering and Industrial Aerodynamics*, 77:53–64.
- 550 Powell, M. D., Vickery, P. J., and Reinhold, T. A. (2003). Reduced drag coeffi-  
551 cient for high wind speeds in tropical cyclones. *Nature*, 422(6929):279–  
552 283.
- 553 Röhrs, J., Christensen, K. H., Hole, L. R., Broström, G., Drivdal, M., and  
554 Sundby, S. (2012). Observation-based evaluation of surface wave  
555 effects on currents and trajectory forecasts. *Ocean Dynamics*, 62(10–  
556 12):1519–1533.
- 557 Schott, F. A., Lee, T. N., and Zantopp, R. (1988). Variability of structure and  
558 transport of the Florida Current in the period range of days to seasonal.  
559 *Journal of Physical Oceanography*, 18(9):1209–1230.
- 560 Shinn, E. A. (1988). The geology of the Florida Keys. *Oceanus*, 31(1):46–53.
- 561 Siadatmousavi, S. M., Jose, F., and Stone, G. (2011). Evaluation of two WAM  
562 white capping parameterizations using parallel unstructured SWAN  
563 with application to the Northern Gulf of Mexico, USA. *Applied Ocean  
564 Research*, 33(1):23–30.

- 565 Sikirić, M. D., Roland, A., Janeković, I., Tomazić, I., and Kuzmić, M. (2013).  
566      Coupling of the Regional Ocean Modeling System (roms) and Wind  
567      Wave Model. *Ocean Modelling*, 72:59–73.
- 568 Smith, N. P. (1982). Response of Florida Atlantic shelf waters to hurricane  
569      David. *Journal of Geophysical Research: Oceans*, 87(C3):2007–2016.
- 570 Stokes, G. G. (1880). On the theory of oscillatory waves. *Transactions of*  
571      *the Cambridge philosophical society*.
- 572 Tolman, H. L. et al. (2009). User manual and system documentation of  
573      WAVEWATCH III TM version 3.14. *Technical note, MMAB Contribution*,  
574      276:220.
- 575 Van Den Bremer, T. and Breivik, Ø. (2018). Stokes drift. *Philosophical Trans-*  
576      *actions of the Royal Society A: Mathematical, Physical and Engineering*  
577      *Sciences*, 376(2111):20170104.
- 578 Villas Bôas, A. B., Cornuelle, B. D., Mazloff, M. R., Gille, S. T., and Arduin,  
579      F. (2020). Wave–current interactions at meso-and submesoscales:  
580      Insights from idealized numerical simulations. *Journal of Physical*  
581      *Oceanography*, 50(12):3483–3500.
- 582 Weisberg, R., Liu, Y., and Mayer, D. (2009). Mean circulation on the west  
583      Florida continental shelf observed with long-term moorings. *Geophys.*  
584      *Res. Lett*, 36:L19610.
- 585 Weisberg, R. H. and Zheng, L. (2006). Hurricane storm surge simulations  
586      for Tampa Bay. *Estuaries and Coasts*, 29(6):899–913.
- 587 Wu, L., Chen, C., Guo, P., Shi, M., Qi, J., and Ge, J. (2011). A FVCOM-  
588      based unstructured grid wave, current, sediment transport model, I.  
589      Model description and validation. *Journal of Ocean University of China*,  
590      10(1):1–8.
- 591 Xian, S., Feng, K., Lin, N., Marsooli, R., Chavas, D., Chen, J., and Hatzikyri-  
592      akou, A. (2018). Brief communication: Rapid assessment of damaged  
593      residential buildings in the Florida Keys after Hurricane Irma. *Natural*  
594      *Hazards and Earth System Sciences*, 18(7):2041–2045.

595 Zedler, S., Niiler, P., Stammer, D., Terrill, E., and Morzel, J. (2009). Ocean's  
596 response to Hurricane Frances and its implications for drag coefficient  
597 parameterization at high wind speeds. *Journal of Geophysical Re-*  
598 *search: Oceans*, 114(C4).

599 Zhang, C., Durgan, S. D., and Lagomasino, D. (2019). Modeling risk of man-  
600 groves to tropical cyclones: A case study of Hurricane Irma. *Estuarine,*  
601 *Coastal and Shelf Science*, 224:108–116.